Handheld ultrahigh speed swept source optical coherence tomography instrument using a MEMS scanning mirror

Chen D. Lu,[1] Martin F. Kraus,[1,2] Benjamin Potsaid,[1,3] Jonathan J. Liu,[1] WooJhon Choi,[1] Vijaysekhar Jayaraman,[4] Alex E. Cable,[3] Joachim Hornegger,[2] Jay S. Duker,[5] and James G. Fujimoto[1,*]

[1]*Department of Electrical Engineering and Computer Science and Research Laboratory of Electronics, Massachusetts Institute of Technology, Cambridge, MA, USA*
[2]*Pattern Recognition Lab and School of Advanced Optical Technologies, University Erlangen-Nuremberg, Erlangen, Germany*
[3]*Advanced Imaging Group, Thorlabs, Inc., Newton, NJ, USA*
[4]*Praevium Research Inc., Santa Barbara, CA, USA*
[5]*New England Eye Center and Tufts Medical Center, Tufts University, Boston, MA, USA*
*jgfuji@mit.edu

Abstract: We developed an ultrahigh speed, handheld swept source optical coherence tomography (SS-OCT) ophthalmic instrument using a 2D MEMS mirror. A vertical cavity surface-emitting laser (VCSEL) operating at 1060 nm center wavelength yielded a 350 kHz axial scan rate and 10 µm axial resolution in tissue. The long coherence length of the VCSEL enabled a 3.08 mm imaging range with minimal sensitivity roll-off in tissue. Two different designs with identical optical components were tested to evaluate handheld OCT ergonomics. An iris camera aided in alignment of the OCT beam through the pupil and a manual fixation light selected the imaging region on the retina. Volumetric and high definition scans were obtained from 5 undilated normal subjects. Volumetric OCT data was acquired by scanning the 2.4 mm diameter 2D MEMS mirror sinusoidally in the fast direction and linearly in the orthogonal slow direction. A second volumetric sinusoidal scan was obtained in the orthogonal direction and the two volumes were processed with a software algorithm to generate a merged motion-corrected volume. Motion-corrected standard 6 x 6 mm^2 and wide field 10 x 10 mm^2 volumetric OCT data were generated using two volumetric scans, each obtained in 1.4 seconds. High definition 10 mm and 6 mm B-scans were obtained by averaging and registering 25 B-scans obtained over the same position in 0.57 seconds. One of the advantages of volumetric OCT data is the generation of en face OCT images with arbitrary cross sectional B-scans registered to fundus features. This technology should enable screening applications to identify early retinal disease, before irreversible vision impairment or loss occurs. Handheld OCT technology also promises to enable applications in a wide range of settings outside of the traditional ophthalmology or optometry clinics including pediatrics, intraoperative, primary care, developing countries, and military medicine.

OCIS codes: (170.4460) Ophthalmic optics and devices; (170.5755) Retina scanning; (170.3880) Medical and biological imaging; (170.4500) Optical coherence tomography; (170.4470) Ophthalmology.

References and links

1. B. E. Robinson, "Prevalence of Asymptomatic Eye Disease Prévalence des maladies oculaires asymptomatiques," Revue Canadienne D'Optométrie **65**, 175 (2003).
2. H. A. Quigley, "Number of people with glaucoma worldwide," Br. J. Ophthalmol. **80**(5), 389–393 (1996).
3. F. Wang, D. Ford, J. M. Tielsch, H. A. Quigley, and P. K. Whelton, "Undetected eye disease in a primary care clinic population," Arch. Intern. Med. **154**(16), 1821–1828 (1994).
4. R. Varma, S. A. Mohanty, J. Deneen, J. Wu, and S. P. Azen; LALES Group, "Burden and predictors of undetected eye disease in Mexican-Americans: the Los Angeles Latino Eye Study," Med. Care **46**(5), 497–506 (2008).
5. S. Rowe, C. H. MacLean, and P. G. Shekelle, "Preventing visual loss from chronic eye disease in primary care: scientific review," JAMA **291**(12), 1487–1495 (2004).
6. E. Y. Wong, J. E. Keeffe, J. L. Rait, H. T. Vu, A. Le, C. McCarty, and H. R. Taylor, "Detection of undiagnosed glaucoma by eye health professionals," Ophthalmology **111**(8), 1508–1514 (2004).
7. S. Garg and R. M. Davis, "Diabetic retinopathy screening update," Clin. Diabetes **27**(4), 140–145 (2009).
8. D. Huang, E. Swanson, C. P. Lin, J. S. Schuman, W. G. Stinson, W. Chang, M. R. Hee, T. Flotte, K. Gregory, C. A. Puliafito, and J. G. Fujimoto, "Optical Coherence Tomography," Science **254**(5035), 1178–1181 (1991).
9. J. S. Schuman, C. A. Puliafito, J. G. Fujimoto, and J. S. Duker, Optical Coherence Tomography of Ocular Diseases, 3rd Edition (Slack Inc., Thorofare, NJ, 2012).
10. S. Radhakrishnan, A. M. Rollins, J. E. Roth, S. Yazdanfar, V. Westphal, D. S. Bardenstein, and J. A. Izatt, "Real-time optical coherence tomography of the anterior segment at 1310 nm," Arch. Ophthalmol. **119**(8), 1179–1185 (2001).
11. W. Jung, J. Kim, M. Jeon, E. J. Chaney, C. N. Stewart, and S. A. Boppart, "Handheld Optical Coherence Tomography Scanner for Primary Care Diagnostics," IEEE Trans. Biomed. Eng. **58**(3), 741–744 (2011).
12. J. T. W. Yeow, V. X. D. Yang, A. Chahwan, M. L. Gordon, B. Qi, I. A. Vitkin, B. C. Wilson, and A. A. Goldenberg, "Micromachined 2-D scanner for 3-D optical coherence tomography," Sens. Actuators A Phys. **117**(2), 331–340 (2005).
13. W. G. Jung, J. Zhang, L. Wang, P. Wilder-Smith, Z. P. Chen, D. T. McCormick, and N. C. Tien, "Three-dimensional optical coherence tomography employing a 2-axis microelectromechanical scanning mirror," IEEE J. Sel. Top. Quantum Electron. **11**(4), 806–810 (2005).
14. W. Jung, D. T. McCormick, J. Zhang, L. Wang, N. C. Tien, and Z. P. Chen, "Three-dimensional endoscopic optical coherence tomography by use of a two-axis microelectromechanical scanning mirror," Appl. Phys. Lett. **88**, 163901 (2006).
15. A. D. Aguirre, P. R. Hertz, Y. Chen, J. G. Fujimoto, W. Piyawattanametha, L. Fan, and M. C. Wu, "Two-axis MEMS scanning catheter for ultrahigh resolution three-dimensional and en face imaging," Opt. Express **15**(5), 2445–2453 (2007).
16. K. H. Kim, B. H. Park, G. N. Maguluri, T. W. Lee, F. J. Rogomentich, M. G. Bancu, B. E. Bouma, J. F. de Boer, and J. J. Bernstein, "Two-axis magnetically-driven MEMS scanning catheter for endoscopic high-speed optical coherence tomography," Opt. Express **15**(26), 18130–18140 (2007).
17. J. Singh, J. H. S. Teo, Y. Xu, C. S. Premachandran, N. Chen, R. Kotlanka, M. Olivo, and C. J. R. Sheppard, "A two axes scanning SOI MEMS micromirror for endoscopic bioimaging," J. Micromech. Microeng. **18**, 025001 (2008).
18. K. Kumar, J. C. Condit, A. McElroy, N. J. Kemp, K. Hoshino, T. E. Milner, and X. Zhang, "Fast 3D in vivo swept-source optical coherence tomography using a two-axis MEMS scanning micromirror," J. Opt. A, Pure Appl. Opt. **10**, 044013 (2008).
19. J. J. Sun, S. G. Guo, L. Wu, L. Liu, S. W. Choe, B. S. Sorg, and H. K. Xie, "3D in vivo optical coherence tomography based on a low-voltage, large-scan-range 2D MEMS mirror," Opt. Express **18**(12), 12065–12075 (2010).
20. D. Wang, L. Fu, X. Wang, Z. Gong, S. Samuelson, C. Duan, H. Jia, J. S. Ma, and H. Xie, "Endoscopic swept-source optical coherence tomography based on a two-axis microelectromechanical system mirror," J. Biomed. Opt. **18**(8), 086005 (2013).
21. R. L. Shelton, W. Jung, S. I. Sayegh, D. T. McCormick, J. Kim, and S. A. Boppart, "Optical coherence tomography for advanced screening in the primary care office," J Biophotonics (2013).
22. B. Potsaid, B. Baumann, D. Huang, S. Barry, A. E. Cable, J. S. Schuman, J. S. Duker, and J. G. Fujimoto, "Ultrahigh speed 1050nm swept source/Fourier domain OCT retinal and anterior segment imaging at 100,000 to 400,000 axial scans per second," Opt. Express **18**(19), 20029–20048 (2010).
23. I. Grulkowski, J. J. Liu, B. Potsaid, V. Jayaraman, C. D. Lu, J. Jiang, A. E. Cable, J. S. Duker, and J. G. Fujimoto, "Retinal, anterior segment and full eye imaging using ultrahigh speed swept source OCT with vertical-cavity surface emitting lasers," Biomed. Opt. Express **3**(11), 2733–2751 (2012).
24. I. Grulkowski, J. J. Liu, B. Potsaid, V. Jayaraman, J. Jiang, J. G. Fujimoto, and A. E. Cable, "High-precision, high-accuracy ultralong-range swept-source optical coherence tomography using vertical cavity surface emitting laser light source," Opt. Lett. **38**(5), 673–675 (2013).
25. A. Unterhuber, B. Povazay, B. Hermann, H. Sattmann, A. Chavez-Pirson, and W. Drexler, "In vivo retinal optical coherence tomography at 1040 nm - enhanced penetration into the choroid," Opt. Express **13**(9), 3252–3258 (2005).

26. Y. Yasuno, Y. J. Hong, S. Makita, M. Yamanari, M. Akiba, M. Miura, and T. Yatagai, "In vivo high-contrast imaging of deep posterior eye by 1- um swept source optical coherence tomography and scattering optical coherence angiography," Opt. Express **15**(10), 6121–6139 (2007).

27. W. Drexler and J. G. Fujimoto, "State-of-the-art retinal optical coherence tomography," Prog. Retin. Eye Res. **27**(1), 45–88 (2008).

28. D. M. de Bruin, D. L. Burnes, J. Loewenstein, Y. Chen, S. Chang, T. C. Chen, D. D. Esmaili, and J. F. de Boer, "In vivo three-dimensional imaging of neovascular age-related macular degeneration using optical frequency domain imaging at 1050 nm," Invest. Ophthalmol. Vis. Sci. **49**(10), 4545–4552 (2008).

29. M. F. Kraus, B. Potsaid, M. A. Mayer, R. Bock, B. Baumann, J. J. Liu, J. Hornegger, and J. G. Fujimoto, "Motion correction in optical coherence tomography volumes on a per A-scan basis using orthogonal scan patterns," Biomed. Opt. Express **3**(6), 1182–1199 (2012).

30. H.-L. Liou and N. A. Brennan, "Anatomically accurate, finite model eye for optical modeling," J. Opt. Soc. Am. A **14**(8), 1684–1695 (1997).

31. American National Standard for Safe Use of Lasers, ANSI Z136.1 (American National Standards Institute, New York, 2007).

32. W. Choi, B. Potsaid, V. Jayaraman, B. Baumann, I. Grulkowski, J. J. Liu, C. D. Lu, A. E. Cable, D. Huang, J. S. Duker, and J. G. Fujimoto, "Phase-sensitive swept-source optical coherence tomography imaging of the human retina with a vertical cavity surface-emitting laser light source," Opt. Lett. **38**(3), 338–340 (2013).

33. B. Cense, N. Nassif, T. C. Chen, M. C. Pierce, S. H. Yun, B. H. Park, B. Bouma, G. Tearney, and J. F. de Boer, "Ultrahigh-resolution high-speed retinal imaging using spectral-domain optical coherence tomography," Opt. Express **12**(11), 2435–2447 (2004).

34. J. F. de Boer, B. Cense, B. H. Park, M. C. Pierce, G. J. Tearney, and B. E. Bouma, "Improved signal-to-noise ratio in spectral-domain compared with time-domain optical coherence tomography," Opt. Lett. **28**(21), 2067–2069 (2003).

1. Introduction

Many retinal diseases remain undetected until irreversible vision loss or impairment occurs because they are asymptomatic in the early stages and patients have limited access to eye care. In a Canadian study of 24,570 optometry patients, 14.4% were found with asymptomatic eye disease even though 66.8% of patients with disease had a best-corrected visual acuity of 20/25 or better [1]. A study of 14 surveys for glaucoma in a predominantly European population revealed that only 45 ± 25% of patients diagnosed with glaucoma were aware of their disease [2]. The rate of undetected retinal disease is especially high for minority communities that do not have easy access to eye care. In East Baltimore, a 1994 study with 405 general medicine patients over the age of 40 of whom 94% were black showed that 50.6% of patients had clinically important ocular pathology and one third of those were unaware of the disease [3]. A study of 6,357 Latinos showed 53% of subjects had eye disease and of those, 63% had undetected eye disease [4]. One method of early detection is to screen elderly individuals for early signs of retinal diseases [5]. If pathology is detected by screening, early treatment can prevent irreversible vision loss [6, 7]. A screening tool must be able to detect retinal pathology with sufficient sensitivity, while remaining easy-to-use and portable so that the screening can be performed outside of the standard ophthalmology or optometry setting.

Optical coherence tomography (OCT) is a non-invasive, non-contact optical imaging technique [8] that has become a standard modality to diagnose and monitor retinal diseases in ophthalmology [9]. However, most commercial OCT systems are bulky and table mounted, limiting their deployment for screening applications. To increase the portability of OCT systems, the galvanometer scanners used in tabletop systems have been adapted for handheld instruments in research [10, 11] and commercial systems. However, galvanometer scanners consist of two orthogonally oriented X and Y servo motors in an aluminum mount, constraining the minimum size and weight of the instruments.

To enable a more portable OCT instrument, microelectromechanical systems (MEMS) mirrors can be used for beam scanning. MEMS mirrors are fabricated using semiconductor technology and can be packaged on a compact integrated (IC) chip. 2D MEMS mirrors that scan in two axes are an alternative to the larger galvanometer scanners and have been used extensively to develop compact probes capable of 3D OCT image generation in endoscopic applications [12–20]. Recently, a 70 kHz spectral domain OCT (SD-OCT) handheld

instrument was developed for primary care applications utilizing a 3.2 mm diameter 2D four-quadrant MEMS scanning mirror for 2D OCT scans in the horizontal and vertical directions [21]. Our work utilizes a similar 2.4 mm diameter 2D MEMS scanning mirror, but uses ultrahigh imaging speed to generate 3D OCT volumetric data of the retina. Volumetric 3D imaging is a significant advance because OCT fundus images and arbitrary 2D images precisely registered to fundus features can be generated from the 3D data set.

Recent advancements in swept source OCT (SS-OCT) technology enable dramatic improvements in handheld OCT device design and performance. SS-OCT has many advantages over SD-OCT including less sensitivity roll-off with depth, higher dynamic range with balanced detection, and no spectrometer losses [22]. Our group has recently demonstrated that 1050 nm wavelength vertical cavity surface-emitting laser (VCSEL) light sources can achieve high speed [23] and long imaging ranges [24]. Higher imaging speed enables denser sampling and the acquisition of volumetric data. Long imaging range simplifies the alignment of a handheld OCT device by making the working distance tolerance less critical. Long imaging range is also important for wide field retinal imaging because of the retinal curvature. Limited imaging range can cause the retina to cross the zero delay and produce mirror image artifacts, or to move outside the imaging range. In addition, images acquired at 1050 nm wavelengths have better penetration and less scattering in tissues compared to images taken at standard 860 nm OCT wavelengths [25–28]. This allows better imaging through cataracts and below the retina into the choroid.

In this manuscript, we report a wide field, ultrahigh speed, handheld swept source OCT (SS-OCT) device which promises to enable applications in settings outside of the ophthalmology and optometry clinics. Two different designs with different enclosures with identical optical components were developed to access comparative ergonomic performance. Both handheld instrument designs contained an iris camera for alignment to the subject's pupil and a fixation target to position the OCT beam scan on the retina. A 3.5 inch LCD screen also provided operator feedback during alignment and acquisition. The swept light source operated at 350 kHz with a 63 nm full range sweep range centered at ~1060 nm, corresponding to a full width half max (FWHM) axial resolution of 10 μm in tissue. Although the VCSEL can sweep a larger wavelength range, the 63nm sweep range was chosen as a compromise between axial resolution and imaging range due to limits in data acquisition bandwidth. The OCT imaging engine was optically clocked and had an imaging range of 3.08 mm in tissue. Volumetric 3D OCT imaging was acquired over standard 6 x 6 mm^2 and wide 10 x 10 mm^2 retinal fields with an acquisition time of 1.4 second per volume scan. Since a handheld device has operator motion in addition to subject motion, motion correction of the data was performed using a software algorithm [29]. The motion correction algorithm uses two input volumes with orthogonal raster scan patterns to estimate motion and generates a motion-corrected, merged volume with improved signal to noise. High definition B-scans were also generated by registering and averaging 25 B-scans acquired in 0.57 seconds at the same location. The combination of these features enables an effective handheld retinal imaging instrument capable of acquiring wide field, motion-corrected 3D OCT volumes and high definition B-scans of the retina.

2. Methods

2.1 Handheld ophthalmic OCT instrument

The requirements for an effective handheld OCT imaging instrument include an ergonomic design, ability to image a wide field of view on the retina, and robust methods to align the device through the pupil and scan the desired region of the retina. For the ergonomic design, the handheld OCT instrument components were housed in a 3D-printed ABS plastic enclosure designed in SolidWorks (Dassault Systèmes) and printed using a 3D printer (Stratasys, Dimension Elite). The optical elements were directly placed in printed sockets in

the plastic to eliminate the need for lens mounts, reducing the weight of the system. Two ergonomically different designs, a power grip and a camcorder style design (Fig. 1), were developed with the same internal optical components.

The power grip style device in Fig. 1(A)-1(B) was designed to be firmly gripped in one hand with adjustments performed by the other hand. A 3.5 inch VGA LCD screen was mounted on the back of the device to display the iris camera video and OCT scans during alignment. To correct for the subject's refractive error, a helical-threaded focus adjustment with a thread pitch of 20 mm was used to translate the last lens set to accommodate refractive errors of −12 to + 6 Diopters over 15 mm of movement. This corresponded to a 2 Diopter change per 30 degrees rotation of the focus adjustment. The instrument also had a fixation light and the operator could manually translate the horizontal position by an adjustment on top of the instrument. The acquisition trigger button was located next to the index finger on the front of the angled grip. A trigger button was used instead of a footswitch in order to reduce the system complexity. The weight of the device was 500 g and the dimensions were 15.1 cm length x 18.2 cm height x 7.4 cm width including the LCD screen.

The camcorder style device in Fig. 1(C)-1(D) was designed for single-handed use. An adjustable nylon strap was attached to the side of the device to support the back of the operator's hand while in operation. The LCD screen was attached to the other side of the instrument. The screen could be tilted vertically to adjust to the viewing angle and folded against the side for storage. An acquisition trigger button on the back of the enclosure could be actuated by the operator's thumb. The operator's ring and little finger rotated the helical-threaded focus adjustment. The adjustment for the fixation light was the same as in the power grip design and could be adjusted with the operator's index finger. The overall weight of this instrument was 420 g and the dimensions were 16.3 cm length x 10.2 cm height x 5.6 cm width with the LCD screen folded and 14.3 cm width with the LCD screen extended. Both devices had advantages and limitations that will be further analyzed in the discussion section.
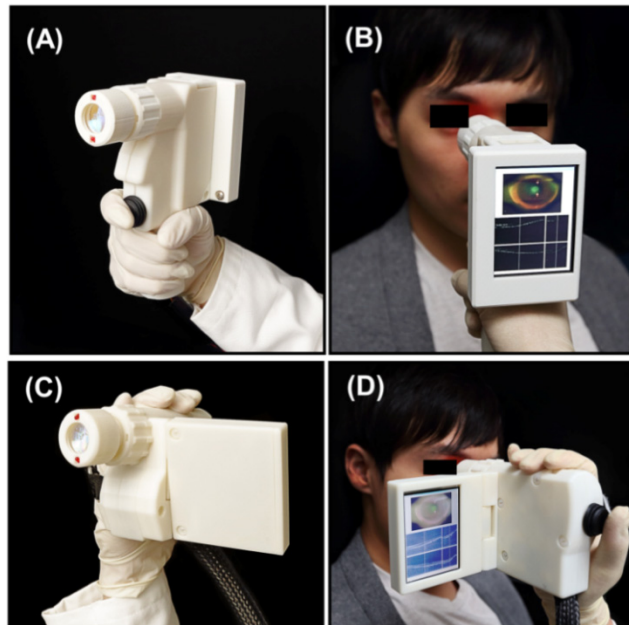

Fig. 1. Photographs of the (A-B) power grip style and (C-D) camcorder style designs. The camcorder design has a nylon strap (not visible in the photographs) which wraps around the back of the operator's hand. The optical components inside both enclosures are identical.

The number of resolvable spots is a key parameter which describes the field of view versus resolution of a scanning system. This is defined as the number of resolvable imaging positions across the scanned field of view. A small number of resolvable spots over a wide field results in poor sampling across the field and small features may not be resolved. The scanning mirror diameter d_m and the optical scanning angle $\pm \theta_m$ determine the number of resolvable spots. Assuming the scanning mirror size accommodates a Gaussian beam at the 5% intensity diameter, such that there is only minimal vignetting by the mirror, then $d_m = 2.45\omega_m$ where ω_m is the Gaussian beam half width at the $1/e^2$ or 13.5% intensity. The diffraction angle for the focused Gaussian beam can be written in terms of the mirror diameter:

$$\theta_{diff} = \tan^{-1}\left(2.45\frac{\lambda_0}{\pi d_m}\right) \approx 2.45\frac{\lambda_0}{\pi d_m} \tag{1}$$

where λ_0 is the center wavelength and θ_{diff} is assumed to be small. We define two spots to be resolved when the angle between two peak intensities is equal to twice the diffraction angle at the $1/e^2$ intensity point. This means the number of resolvable spots can be defined as the total scanning angle divided by twice the diffraction angle:

$$NRS = 2\theta_m \big/ 2\theta_{diff} = \pi\theta_m d_m \big/ 2.45\lambda_0 \tag{2}$$

The MEMS mirror has a 2.4 mm diameter with a $\pm 10°$ optical scanning angle and at 1060 nm would theoretically have 507 resolvable spots.

The optical components for the OCT sample arm design in Fig. 2(A) were modeled in ZEMAX (Radiant Zemax) using an eye model [30] to optimize the imaging performance. The output of a 1.5 m optical fiber was collimated by a 9 mm focal length, 6 mm diameter lens. The collimated beam had a 2.07 mm ($1/e^2$ diameter) beam with an 18° angle of incidence on the 2.4 mm diameter gold-bonded mirror 2D MEMS scanner (Mirrorcle Technologies Inc.). The MEMS scanner had a 670 Hz resonance frequency in the X and Y axes. The MEMS scanner was driven with differential voltages of 0-100 V generated by a high voltage amplifier (Mirrorcle Technologies Inc.). A digital to analog (D/A) board (National Instruments) provided the input voltages to the amplifier. The telescopic arrangement of lenses after the MEMS scanner consisted of a 50 mm focal length, 12.7 mm diameter achromat for the relay lens and a pair of 50 mm focal length, 25.4 mm diameter achromats for the ocular lens. The incident beam on the cornea was 0.91 mm ($1/e^2$ diameter) resulting in a spot size of 23.7 μm ($1/e^2$ diameter) on the retina. The working distance from the ocular lens surface to the subject's eye was approximately ~22 mm, depending on the subject's refraction. The MEMS scanner had a maximum optical scan angle of $\pm 10°$ which, after angle magnification, produced a scan angle of $\pm 21.3°$ incident on the cornea, corresponding to $\pm 15.8°$ about the pupil (accounting for corneal curvature and index of refraction in the eye model), producing a 12 mm scan length on the retina. The number of resolvable spot sizes using this eye model is calculated by dividing the total scan length by the spot size diameter, yielding 507 spots, which agrees with the theoretical value calculated above. The measured incident power on the eye was 1.85 mW which is within the American National Standard for Safe Use of Lasers (ANSI) standards for safe retinal exposure at 1060 nm [31].

The OCT beam was aligned through the pupil and the scan positioned on the retina using an iris camera and a manual fixation target, respectively. For the iris camera pathway shown in Fig. 2(B), the light from the anterior eye propagated through the ocular lens and a dichroic mirror that transmitted the visible and reflected the near infrared OCT beam. The visible light was collected by a 45 mm focal length, 25.4 mm diameter achromat and a 50 mm focal length biconvex lens. After reflecting from a 50:50 visible beam splitter, the light was collimated with a 30 mm focal length, 12.7 mm diameter achromat into a webcam (Microsoft LifeCam) with an auto focus lens. The webcam imaged a 1.2 cm diameter area of the subject's iris and

pupil. A pair of angled red LED diodes on the OCT instrument lens illuminated the iris. To position the OCT scan on the retina, a fixation target was used as shown in Fig. 2(C). The fixation target consisted of a single flat top green LED and a 7.5 mm focal length, 5 mm diameter achromat lens that directed the light through the 50:50 visible beam splitter. The optics after the beam splitter were identical to those used for the iris camera. The fixation LED and lens could be manually actuated ± 6 mm horizontally to produce a ± 11° shift in the image on the retina. This enabled aiming the OCT scan on the retina to positions between the fovea and optic nerve head.
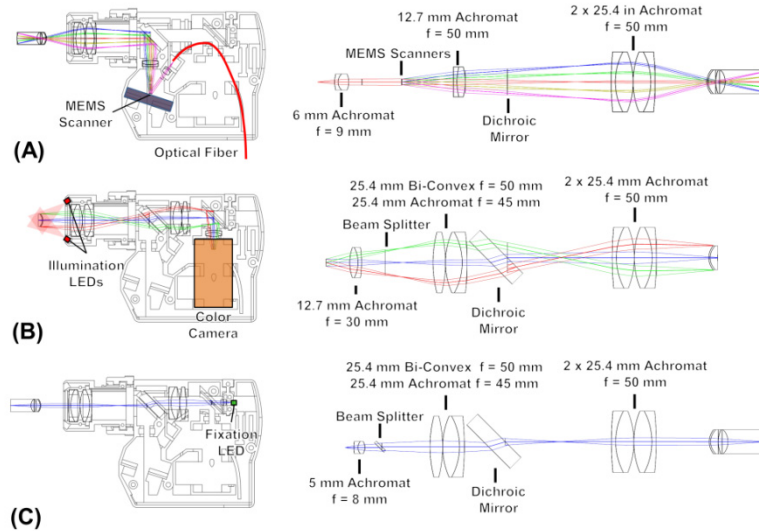
Fig. 2. Handheld OCT instrument internal optical layout and unfolded optical components showing the (A) OCT 1060 nm optical path, (B) iris camera visible optical path, and (C) fixation target visible optical path.

2.2 Ultrahigh speed swept source imaging system

Figure 3 shows a schematic diagram of the SS-OCT imaging engine for the handheld ophthalmic instrument. The light source, OCT interferometer and reference arm were in a separate unit from the handheld instrument. The swept light source was a vertical cavity surface emitting laser (VCSEL) light source (Praevium/Thorlabs, Inc.) centered at ~1060 nm and frequency swept sinusoidally at 350 kHz. The VCSEL output was amplified by a semiconductor optical amplifier (SOA) (not shown) and modulated with a 60% duty cycle to generate a unidirectional long to short wavelength sweep. The full sweep range was 63 nm yielding a measured axial resolution of 10 μm FWHM in tissue.

The VCSEL output was split with a 90:10 coupler so that 10% of the light was directed to a calibration Mach-Zehnder interferometer (MZI). The MZI consisted of two 50:50 couplers and 4 collimator lenses with an adjustable optical path delay difference between the two MZI arms, using matched optical fiber lengths in the two MZI arms for dispersion balancing. The MZI output was detected with a prototype combined 1.8 GHz balanced photodetector and discriminator (Thorlabs, Inc.). The MZI path length difference was set to 8.2 mm to generate a digital optical clock that triggers the OCT signal data acquisition on equally spaced frequency or wavenumber intervals, as described previously in reference [32]. The OCT signal from each frequency sweep could then be directly Fourier transformed without the need to resample from uniform time to uniform frequency or wavenumber.

The remainder of the VCSEL output went to the OCT interferometer which consisted of an 80:20 coupler which collected 80% of the return signal from the sample arm into the detectors. The reference arm consisted of two collimators with dispersion compensating glass

in the optical path and a translating retroreflector to set the zero delay. An additional fiber length was used in the reference arm to match the sample arm round trip fiber length.

The returning light from the sample and reference arms were interfered with a 50:50 coupler and detected by a prototype 1.5 GHz dual balanced photodetector (Thorlabs, Inc.). The OCT signal from the detector output was filtered with a 490 MHz low pass filter (Mini-Circuits) to remove high frequency noise that may be aliased to the sampled frequencies. The filtered OCT signal was digitized by a high speed A/D card (Alazartech, ATS9360) and processed with software written in C++ on an Intel Core i7 computer. The A/D card was specified for 1.8 GBPS acquisition rates using fixed internal clocking, but could only operate up to 1.2 GBPS rates when using a variable sampling frequency from an external optical clock generated by the MZI. The MZI for the optical clock was set to an 8.2 mm path length difference in air, such that the optical clock had a maximum frequency of 1.2 GHz. This produced a measured imaging range of 4.1 mm in air, corresponding to 3.08 mm in tissue. The A/D card was repeatedly triggered synchronously with the VCSEL frequency sweep to acquire 928 samples between the long to short sinusoidal wavelength sweep. The acquisition occurred during 75% of the time the SOA was enabled per sweep.

The OCT fringe signal was multiplied by a complex phase correction factor to compensate dispersion mismatch in the OCT interferometer [33]. The 928 equally wavenumber-spaced samples in each sweep were zero-padded with an additional 928 samples. The combined 1856 samples were directly Fast Fourier Transformed and converted to log intensity. Due to the symmetry of the Fourier transform, half of the transformed data was used for the 928 pixels per A-scan. The axial pixel spacing was 4.4 um in air, corresponding to 3.3 um in tissue.

The images were further processed to compensate for the non-uniformity of the MEMS sinusoidal sweep trajectory. The sinusoidally swept B-scans were resampled into linearly spaced A-scan positions by averaging sinusoidal A-scans using a Gaussian filter function with its peak centered at each linearly spaced point and a standard deviation of 0.5 linearly spaced points. This standard deviation value was chosen to prevent blurring of adjacent A-scans. Once the volumes were linearized, the two orthogonally scanned volumes were motion-corrected with a software algorithm [29] using a Core i7-3970K CPU (Intel) running at 3.2 GHz and a GeForce GTX 680 video card (Nvidia). After motion-correction, the two volumes were merged to increase the signal to noise. The processing time for two 350 x 350 A-scan orthogonal volumes was approximately 1.5 minutes. When repeated B-scans were acquired to generate a high definition 2D image, the 2D cross sections were registered and averaged.
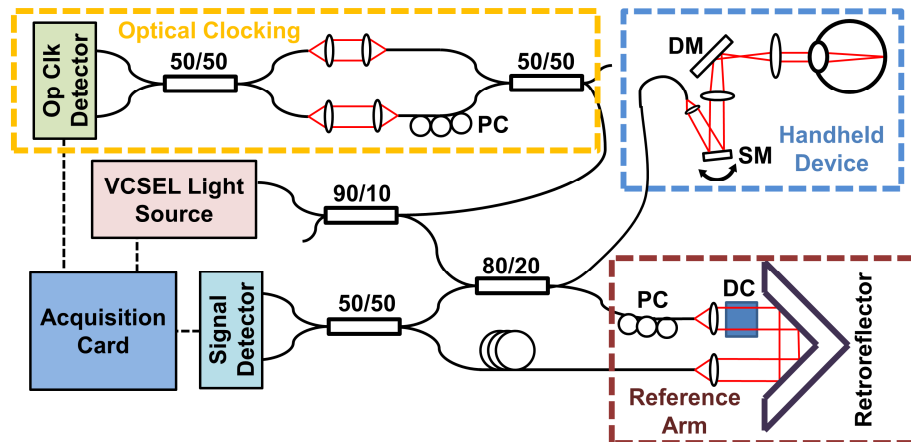

Fig. 3. Swept Source OCT system at 1060 nm using a VCSEL swept source light source. A calibration MZI is used to generate an optical clock signal. MEMS scanning mirror (SM). Dichroic mirror (DM). Polarization controller (PC). Dispersion compensation glass (DC).

2.3 Imaging protocol

Five normal healthy subjects with a mean age 26.2 (range 23 to 31 years) were imaged with the camcorder style device. Written informed consent was obtained prior to the study and imaging was performed according to protocols approved by the MIT Committee on the Use of Humans as Experimental Subjects (COUHES). Each subject was seated in a chair with a headrest and with the back of their head against the headrest. The operator was seated on the side of the subject. The operator first set the fixation target to the desired retinal imaging region. The device was aligned to the subject's eye and centered to the pupil using the video displayed from the iris camera. During OCT alignment, a set of three horizontal OCT B-scans at the top, middle, and bottom of the scan area and one vertical B-scan bisecting the scan area were continuously acquired and displayed, similar to the alignment B-scans on commercial OCT instruments (Zeiss Cirrus OCT). Once the device was aligned to the pupil, the operator moved the device forwards and backwards in the axial direction until the retinal layers could be seen in the preview scans. The operator then adjusted the focus to maximize the OCT signal from the subject's retina. To adjust the orientation of the 2D scans, the operator rotated the instrument about the OCT beam axis. Since the subject's gaze was directed to the fixation target, rotating the hand held instrument caused the B-scan to rotate radially about the fovea. Once the images from the OCT preview were satisfactory, the operator pressed the acquisition button on the device to start the acquisition scan.

Four sets of scan patterns were acquired using the handheld instrument. Because of the fast sweep repetition rate of the VCSEL light source and the limited resonant frequency of the MEMS mirror, sinusoidal raster scans were performed. To raster scan an area of the retina for volumetric data acquisition, the beam was scanned sinusoidally in one transverse direction and scanned at a constant velocity in the other direction. Each sinusoid scan period contained a forwards and backwards B-scan. To interleave the forward and backward sinusoidal B-scans, the OCT data was shifted an integer number of A-scans, and this integer shift remained constant through all the acquisitions. A second orthogonal sinusoidal raster scan with the fast and slow scan axes reversed was then acquired. Standard 6 x 6 mm^2 area, 1400 x 350 A-scan volumes were acquired of the macula and optic nerve head individually. Wide field volumes over a 10 x 10 mm^2 area of the retina consisting of 1400 x 350 A-scans were acquired in 1.4 seconds, centered between the fovea and optic nerve head. Additionally, 10 mm long, high definition, 8000 A-scan horizontal B-scans across the retina were repeatedly acquired to obtain 25 B-scans scans in 0.57 seconds. The same 2D scan protocol was also performed for 6 mm long B-scans.

During acquisition, the software displayed individual OCT B-scan images processed in real time as the OCT was acquired. This provided an immediate assessment of the OCT data quality and instrument positioning in case of vignetting or axial misalignment. The raw OCT image data with selectable horizontal or vertical cross-sections indicated on an OCT fundus projection, as well as en face images at different depths, was available for visualization within 10 seconds after acquisition before further processing for resampling and motion correction.

3. Results

The images shown were acquired using the camcorder design. Since the internal components in both enclosures were identical, these images are similar to data that can be acquired from the power grip design instrument. The measured sensitivity was 93.8 dB (peak intensity divided by the standard deviation of the noise away from the peak) using a calibrated ND filter and a reflection from a silver mirror. Since the OCT signal was acquired during 75% of the time the SOA was on, the shot noise-limited theoretical sensitivity of the system—given the 1.39 mW effective power, 350 kHz imaging speed, the 1060 nm detector responsivity of 0.7 A/W, the 80% sample arm coupling ratio, a 65% fiber to air sample arm coupling efficiency, three FC/APC couplers with coupling efficiencies of ~90% each, and a 97% silver

mirror reflectivity at 1060nm—was 95.0 dB [34]. Over the 4.1 mm imaging range in air, the 3 dB and 6 dB sensitivity roll-off distances were 2.7 mm and 3.3 mm, respectively. The sensitivity roll-off was not limited by the coherence length of the VCSEL light source so the roll off distances can be lengthened by increasing the detector bandwidth. The overall imaging range can be extended by increasing the number of samples per wavenumber in a sweep by increasing the A/D sampling rate, reducing the imaging speed, or shortening the sweep range [23, 24].

Figures 4, 5, and 6 demonstrate the steps to obtain a motion-corrected volume starting from the sinusoidally scanned volume. Figure 4 shows two representative 6 x 6 mm^2, 1400 x 350 A-scan orthogonal sinusoidal raster scanned OCT volumes of the optic nerve head of a 23 year old subject. The OCT scan was aligned to the optic nerve head by adjusting the fixation target position. Each volume was acquired in 1.4 seconds. The image distortion caused by the non-uniform sinusoidal scans can clearly be seen as a stretched appearance at the edges of the images in the fast sinusoidal scanning direction. Figure 4(A) shows an OCT fundus image from a volume acquired using a horizontal sinusoidal raster scan, with distortion evident on the left and right edges. Conversely, Fig. 4(C) shows an OCT fundus image from a volume acquired using a vertical sinusoidal raster scan, with distortion on the top and bottom edges. Distortion is not evident in the orthogonal directions to the fast sinusoidal scan, where the beam is linearly scanned. The OCT fundus in Fig. 4(A) also shows a motion artifact causing a discontinuity in the vessel pattern. Figure 4(B) shows a vertical cross section extracted from the slow scan direction of the horizontal sinusoidal raster scan of Fig. 4(A) showing axial motion artifacts but no stretching distortion in the slow linear scan direction. Two sets of motion artifacts are seen in Fig. 4(C). The leftmost motion artifact created a repeated scan of the same area, distorting the shape of the optic nerve head. The rightmost motion artifact caused a discontinuity in the vessel pattern similar to the motion artifact in Fig. 4(A). Figure 4(D) shows a vertical cross section from the fast sinusoidal scan direction of the vertical raster scan of Fig. 4(C) showing little axial motion artifact, but distortion on the edges caused by the sinusoidal scan.

Figure 5 shows the two volumes displayed in Fig. 4 after sinusoidal to linear resampling. The motion artifacts in the previous fundus images are still present in Figs. 5(A) and 5(C). However the stretching distortion at the top and bottom edges of the vertical raster in Fig. 4(A) and the left and right edges of the horizontal raster in Fig. 4(C) has been corrected by the resampling. Figure 5(B) shows the cross section in the slow direction at the same position as in Fig. 4(B) with the same axial motion artifacts. Figure 5(D) shows the linearized vertical cross section with corrected distortion on the edges of the scan. Figures 5(B) and 5(D) have improved signal to noise compared to Figs. 4(B) and 4(D) due to the averaging of neighboring A-scans when resampling the 1400 sinusoidal A-scans to 350 linear A-scans.
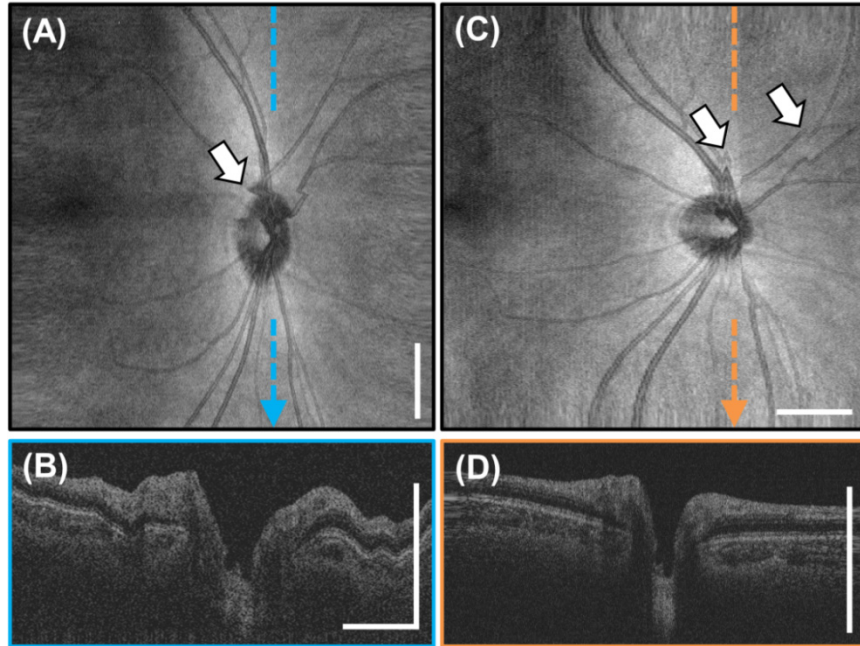
Fig. 4. 6 x 6 mm^2, 1400 x 350 A-scan sinusoidally raster scanned volumes of the optic nerve head acquired in 1.4 seconds each. (A) OCT fundus of the horizontal sinusoidal raster scan. (B) Indicated cross section. (C) OCT fundus of the vertical sinusoidal raster scan. (D) Indicated cross section. Arrows indicate motion artifacts. Scale bars are not displayed in the sinusoidally scanned directions due to nonlinear spacing. Scale bars are 1 mm.
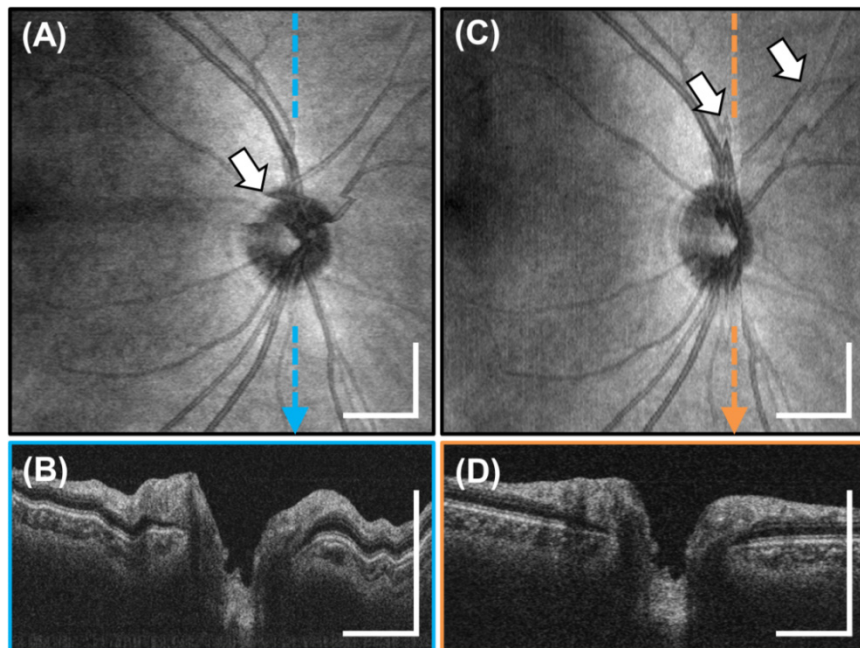

Fig. 5. 6 x 6 mm^2, 350 x 350 A-scan volumes after sinusoid to linear resampling of the volumes in Fig. 4. (A) OCT fundus of linearized horizontal raster scan. (B) Indicated cross section. (C) OCT fundus of linearized vertical raster scan. (D) Indicated cross section. Arrows indicate motion artifacts. Scale bars are 1 mm.

Figure 6 shows the result from motion correction and volume averaging of the two linearly resampled volumes as displayed in Fig. 5. Notice that the motion artifacts indicated in the fundus images of the previous figures have been corrected in the motion-corrected fundus image in Fig. 6(A). The discontinuous vessel patterns on the fundus image and the region of the repeated scan in the vertical raster volume have been mended. The cross sections in Fig. 6(B)-6(C) are free from axial motion. Compared to Figs. 5(B) and 5(D), Fig. 6(C) has higher signal to noise due to the averaging of the two motion-corrected volumes.
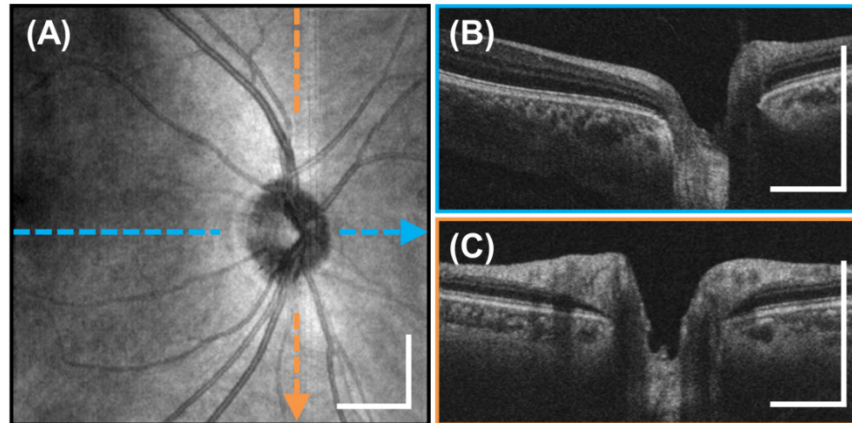
Fig. 6. Motion-corrected 6 x 6 mm^2, 350 x 350 A-scan volume of the optic nerve head generated from two linear raster scanned volumes from Fig. 5. (A) En-face OCT fundus image. (B-C) Horizontal and vertical cross sectional images indicated by the colored lines. Scale bars are 1 mm.

Figure 7 shows a 6 x 6 mm^2, 350 x 350 A-scan motion-corrected, volumetric OCT of the macula of a 31 year old subject generated using the same method described previously. Figure 5(A) shows an OCT fundus view and Figs. 7(B)-7(C) show horizontal and vertical cross sections extracted from the motion-corrected volume.
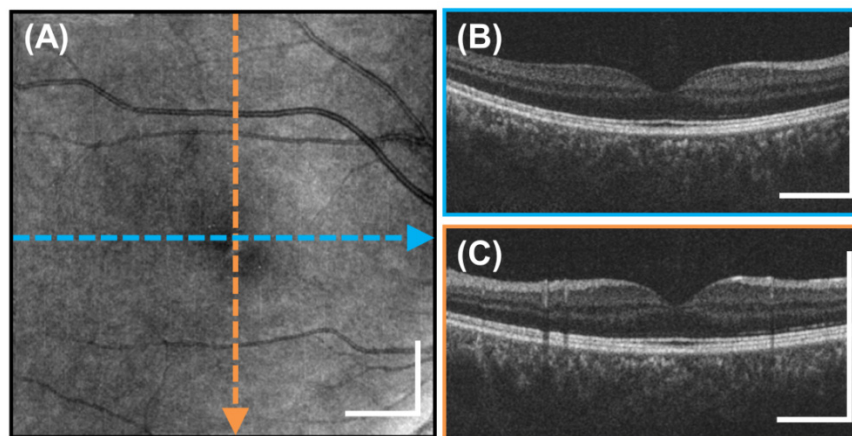

Fig. 7. Motion-corrected 6 x 6 mm^2, 350 x 350 A-scan volume of the macula generated from two raster scanned volumes acquired in 1.4 seconds per volume. (A) En-face OCT fundus image. (B-C) Horizontal and vertical cross sectional images indicated by the colored lines. Scale bars are 1 mm.

Figure 8 shows a representative wide field, 10 x 10 mm^2, 350 x 350 A-scan motion-corrected, volumetric OCT from a 27 year old subject. Figure 8(A) shows the OCT fundus view generated by summing the volume in the axial direction. The wide field volume includes

both the macula and optic nerve head, enabling a simple imaging protocol which can screen for pathology in both of these key locations. The image quality of OCT fundus view in Fig. 8(A) is better than commercial OCT instruments because of the larger number of A-scans and approaches fundus camera image quality. A motion-corrected horizontal cross section is shown in Fig. 8(B). Two motion-corrected, vertical cross sections are shown in Figs. 8(C) and 8(D) intersecting the optic nerve head and macula, respectively. The correction of motion artifacts in both directions enables arbitrary motion-corrected cross sections in any direction or shape to be extracted from the volumetric data. Figure 8(E) shows a 3.4 mm diameter circumpapillary cross section, used for glaucoma diagnosis, extracted from the motion-corrected volume.

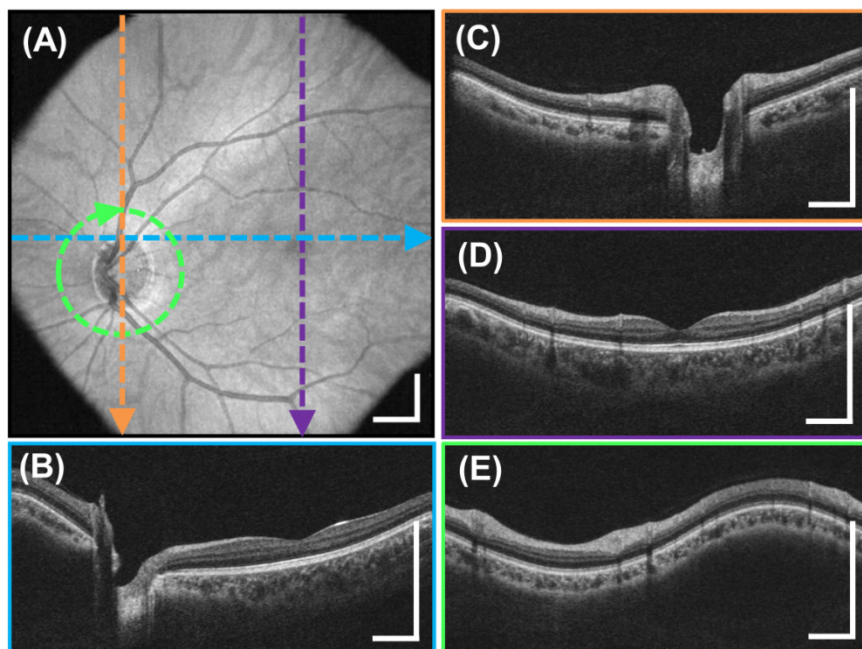

Fig. 8. Motion-corrected, wide field 10 x 10 mm^2, 350 x 350 A-scan volume generated from two raster scanned volumes acquired in 1.4 seconds each. (A) En-face OCT fundus image. (B-D) Color-indicated cross sections on the fundus. (E) Interpolated 3.4 mm diameter circumpapillary scan extracted from motion-corrected volumetric data. Scale bars are 1 mm.

High definition, individual 10 mm cross-sectional OCT images were generated by oversampling and averaging multiple B-scans. Figure 9(A) shows an example high definition image acquired of a 25 year old subject in 0.57 seconds. The original 8000 A-scan sinusoidally scanned cross section was repeated 25 times. Each B-scan was resampled to a linear 2000 A scan cross-sectional image. The 25 repeated B-scans were then registered and averaged to increase signal and reduce speckle noise. This enables the acquisition of high definition cross-sectional images of areas of interest, similar to scanning protocols in commercial OCT systems. The high definition images enable visualization of retinal structure and should facilitate diagnosis of retinal pathologies. The enlarged images in Figs. 9(B)-9(C) show the deep image penetration achieved by long wavelength 1060 nm light and the higher signal level from image averaging which enables visualization of the choroid and sclera.
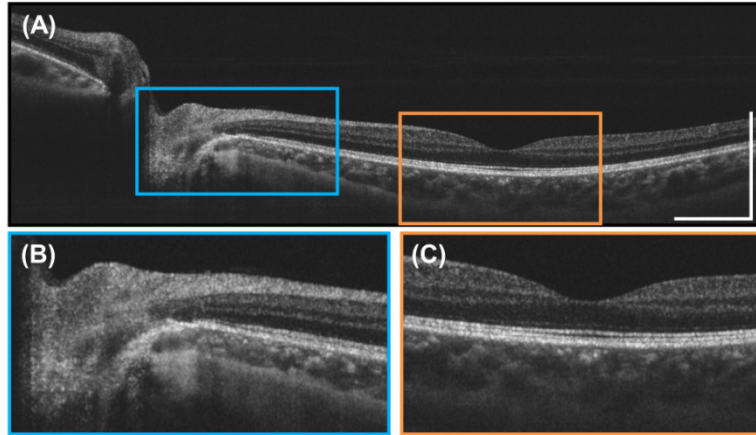
Fig. 9. (A) High definition, 10 mm long 2000 A-scan image generated by repeatedly scanning the same position 25 times in 0.57 seconds and then registering and averaging the B-scans. (B) Enlarged image near the optic nerve head. (C) Enlarged image of the foveal region. Scale bars are 1 mm.

The cross sectional images in the previous figures were cropped in the axial direction to better display the retina and do not show the full 3.08 mm imaging range of the system in tissue. Figure 10 shows three full axial range images with the retina at different axial positions. The figures show 6 mm long high definition images generated by registering and averaging 25 B-scans acquired from a different 25 year old subject. These images demonstrate the long imaging range of the VCSEL swept source OCT. Long imaging range without appreciable sensitivity roll-off is an important advantage for a handheld device facilitating ease of alignment, wide field imaging, and reduced sensitivity to axial positioning during acquisition.
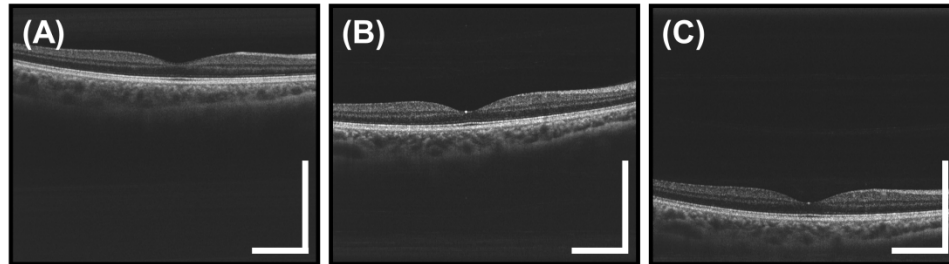

Fig. 10. Full axial range, high definition 6 mm long 2000 A-scan images of the macula obtained from 25 registered and averaged repeated B-scans. (A-C) The images show the retina at various depths and demonstrate the 3.08 mm imaging range in tissue. Notice the lack of severe sensitivity roll-off at deeper depths enabled by the VCSEL SS-OCT light source. Scale bars are 1 mm.

4. Discussion

We developed a wide field of view, high speed SS-OCT handheld imaging instrument for ophthalmic retinal imaging. We demonstrated the highest imaging speed to date in a handheld OCT instrument, enabling volumetric data acquisition and high definition cross sectional imaging. The ability to acquire 3D volumetric data using a handheld instrument is an important advance because OCT fundus images can be generated and arbitrary cross-sectional images as well as topological retinal layer thickness maps can be extracted from the volumetric data, enabling precise registration to fundus features. This solves one of the major limitations of handheld instruments, mitigating the requirement of precisely aiming the

instrument scan to a specific position on the retina. SS-OCT with the VCSEL light source provides a long imaging range and reduced sensitivity roll-off which reduces axial positioning requirements and simplifies alignment. The long imaging range also supports wide retinal imaging fields since the retinal curvature does not cause the retina to be outside of the imaging range during scanning.

To make the device compact and light weight, a 2D MEMS scanning mirror was used instead of a galvanometer mirror pair for OCT beam scanning. The MEMS mirror specifications determine the number of resolvable spots and the B-scan rate. The number of resolvable spots is the number of unique points that can be scanned accounting for the scan angle and beam diffraction. The number of resolvable spots is proportional to the mirror diameter times the scan angle and is invariant with changes in the instrument magnification determined by the lenses after the scanning mirror. Increasing either the MEMS mirror size or scan angle would increase the number of resolvable spots. This would support a combination of a larger beam diameter incident on the eye, enabling a smaller focal spot on the retina, or a larger incident scan angle, enabling a wider field of view. A larger beam diameter on the eye also gives a larger numerical aperture (NA) to collect scattered light from the retina, increasing the collection efficiency. However, a larger beam is also more susceptible to vignetting by the iris, making alignment more sensitive to avoid attenuating signal on the edges of wide field images. A smaller beam diameter was chosen for the handheld instrument design because this makes alignment simpler and reduces vignetting, so that wide field volumetric data sets can be acquired more reliably.

The B-scan repetition frequency is limited by the MEMS mirror resonance frequency. The B-scan frequency must be set well below the resonance frequency in order to prevent parasitic excitation of the resonance which generates image distortion. Parasitic excitation of the resonance can occur along the rapid sinusoidally scanning axis of MEMS scans as well as along the perpendicular, slow scanning MEMS axis. The MEMS mirror resonance frequency is determined by the mirror inertia and scales approximately as the inverse square of the mirror diameter. Doubling the mirror diameter generally reduces the resonance frequency by one fourth, resulting in a slower scan repetition frequency. Slower scan repetition frequency limits the number of B-scans in a volume because there is a maximum time that a subject can stably fixate without saccades or blinking. All of these parameters must be carefully considered when choosing the correct MEMS scanning mirror for a handheld OCT instrument.

One of the main limitations for volumetric OCT data acquisition with the MEMS scanning mirror arises because it is necessary to use a sinusoidal scan. Sinusoidal scanning is less efficient compared to linear scanning because at the center of the B-scan, the scan is the fastest with low A-scan densities and at the edges of the B-scan, the scan is the slowest with high A-scan density. In contrast, a linear scan trajectory would yield equally spaced A-scans. However, linearizing the scan requires driving the MEMS with higher harmonics of the scan frequency which causes parasitic excitation of the MEMS resonance frequency since the MEMS scanners did not have a closed loop feedback system. The ultrahigh 350 kHz axial scan rate provided by the VCSEL swept laser allowed a large number of A-scans per sinusoidal B-scans, so that even the least sampled portions of the sinusoidal scan had sufficient A-scan density. However the scanning was inefficient. The current handheld instrument acquired 1400 non-uniformly spaced A-scans during one half of the sinusoidal trajectory which were resampled and averaged to 350 uniformly spaced A-scans for each B-scan. A-scan densities could be dramatically improved if the sinusoidal scan trajectory could even be partially linearized. Conversely, improving the scan linearity would relax the requirement for an ultrahigh A-scan rate. In comparison to MEMS mirrors, galvanometer scanners have a speed advantage in scanning linear trajectories and support scanning larger beams and scan angles. For rapid OCT volumetric acquisition, galvanometers can scan a 4 mm diameter beam using an 85% duty cycle linear unidirectional (saw tooth) scan with a

sweep rate of 456 Hz [32], more than 3 times the sweep rate of 125 Hz for the volumes generated by the 2D MEMS. Galvanometers also have better performance because they operate in a closed loop using position feedback to correct the drive waveform instead of open loop for MEMS devices. However, when compared to MEMS mirrors, galvanometer systems are higher cost and relatively larger and heavier due to the aluminum mounting needed for heat dissipation. This manuscript demonstrated that it is possible to acquire volumetric retina data using current MEMS scanning technologies which have advantages and limitations compared to galvanometer systems. Ergonomics is a critical issue for a handheld device. An easy to use device would enable rapid alignment and data acquisition, reducing the time required per imaging session. Two different designs were developed for the device and each had advantages and limitations. The power grip device supported ambidextrous operation, but required two hands for the adjustment of focus and fixation target. In addition, the large height difference between the optical axis of the OCT beam and the operator's wrist acted as a lever, making the alignment overly sensitive to the operator's hand movements. When gripping the instrument, the center of gravity was located forward from the wrist. Therefore, the instrument would tilt forwards if the operator did not actively correct the balance. This tilt could cause misalignment by changing the angle and axial length into the eye amplified by the distance between the wrist and optical axis. Future designs can correct this by moving the optical axis closer to the grip and by redistributing the weight of the instrument. In the camcorder style design, the operator held the instrument on one side. In this position, the wrist was closer to the OCT optical axis, reducing the coupling between hand movements and OCT beam alignment compared to the power grip design. The center of gravity of the camcorder style instrument was directly over the wrist so it did not have the balancing issue described previously. Also, the focus and fixation target adjustments could be actuated with one hand, simplifying operation. However, the camcorder device can only be operated with the right hand, which caused the foldout LCD screen to block the subject's right eye while imaging the left eye. The advantages and limitations of these two designs need to be assessed by imaging subjects in the intended setting in order to fully optimize the ergonomics for future handheld OCT instruments.

The iris camera and fixation target are key components for ease of alignment. The iris camera enabled the instrument to be aligned in stages. Centering the pupil in the iris camera required alignment in the transverse directions. Once the pupil was aligned, the device was moved in the axial direction until the retina could be seen in the OCT previews. The LCD screen on the device displaying the iris camera video and OCT previews provided immediate alignment feedback to the operator. Due to the limited illumination from the red LEDs, the iris camera had some difficulties distinguishing the border between the pupil and dark colored irises. This can be solved in future systems by displaying a crosshair or circles to align the iris and sclera borders. The fixation target also reduced the effects of instrument motion. Because the subject's eye was constantly fixated, the eye followed the fixation target if there was a slight tilt in the instrument caused by the operator. This ensured that the OCT was still scanning the same position on the retina after the tilt. However, this effect must be further tested in elderly subjects who may have difficulties fixating. The fixation target is also essential for the alignment of 2D high definition scans. Rotation of the instrument about the OCT beam rotates the B-scan radially about the fovea. Large angle rotations of the instrument about the OCT beam may cause difficulties in operating the instrument. For future instruments, a 2D translating or LCD screen fixation target may provide more accurate B-scan positioning, but these fixation targets would still need to be easily adjustable by the operator.

Operator motion compounds the effects of motion in a handheld OCT device in addition to subject motion. As mentioned previously, proper ergonomics and ease of alignment aid in reducing operator motion. Pressing the acquisition button resulted in a small transient motion. The motion is small because the push button is an electrical contact that requires minimal

actuation force. If the operator is well trained, the dominant source of motion will be from the subject. Subjects will differ significantly in their ability to maintain a stable head position as well as eye fixation. In addition, motion from unstable fixation will be much faster and more discontinuous that operator motion.

The software motion correction was a critical part of the imaging protocol to remove the effects of motion caused by operator and subject. The use of software motion correction avoids the need for eye tracking hardware and greatly simplifies the instrument design. The major limitation of the software based motion correction method used in this paper is that it requires the acquisition of two orthogonal raster scanned volumes in order to estimate and correct motion. However, the ability to merge the two motion-corrected volumes improves signal and reduces speckle in a manner similar to image averaging. The current algorithm was designed to be flexible for research purposes and allowed processing data from different OCT systems with varying scan protocols. Since this was a preliminary research study to demonstrate the feasibility of a prototype device, the software was not fully optimized for the handheld system, resulting in a processing time of 1.5 minutes. If the software algorithm is optimized for a fixed system configuration and scan protocol such as in a commercial system, the processing time can be reduced to below 30 seconds. The processing time will also become faster with improvements in computer hardware.

Currently, there are two commercial handheld OCT systems that are FDA approved for retinal imaging. Table 1 lists the specifications of the Bioptigen Envisu and Optovue iVue in comparison to the prototype handheld system described in this paper. The prototype SS-OCT handheld instrument had a much higher A-scan rate of 350 kHz, more than 10 times that of the Envisu. The extremely high speed of our prototype enabled acquisition of densely sampled volumetric data sets which were processed to generate motion-corrected volumes. From these volumes, arbitrary cross sections can register to the OCT fundus image. The prototype handheld system also had a longer imaging range and operated using SS-OCT so it did not suffer from the severe sensitivity roll-off of SD-OCT systems. However, the prototype system had worse axial resolution compared to the commercial systems. The prototype SS-OCT system imaged at ~1060 nm wavelength which has been demonstrated to have greater penetration through cataracts and enable better visualization of the choroid compared to the ~840 nm wavelength used by the commercial systems. The 2D MEMS scanning mirrors used in the prototype handheld instrument were much smaller and lighter than the galvanometer scanners in the commercial systems. This was reflected in the prototype handheld's smaller dimensions and much lower weight compared to the commercial systems. Our prototype was similar to the Envisu by having a manual adjustment for correcting for refractive errors, while the iVue has a motorized stage for auto-correction. Automatic correction would reduce the complexity of aligning the device in subjects with varying refractive errors. Our prototype handheld instrument was similar to the iVue by including an LCD display so that the operator could look at the instrument and preview images while aligning. Furthermore, our instrument had a camera and fixation target in addition to the OCT preview scans for alignment analogous to the iVue. The camera allowed the operator to align the OCT beam through the pupil before adjusting the axial position required for the OCT preview to display an image. The fixation target enabled imaging of different areas of the retina without rotating the instrument. Lastly, the commercial systems have various attachments that allow the instruments to image the anterior segment in addition to the retina. The prototype handheld instrument was only demonstrated for retinal imaging but it is possible to implement an adjustable lens configuration to telemetrically scan the anterior segment for future designs.

Table 1. Comparison of Commercial Handheld OCT Systems to the Prototype Handheld OCT System

Specification	Bioptigen Envisu	Optovue iVue	Prototype Handheld
OCT Technology	SD-OCT	SD-OCT	SS-OCT
Imaging Speed	32,000 A-scan/s	26,000 A-scan/s	350,000 A-scan/s
Imaging Range in Tissue	1.7 mm (C2200) 2.5 mm C2300)	2 – 2.3 mm	3.08 mm
Axial Resolution in Tissue	6 µm (HR source) 3 µm (VHR source)	5 µm	10 µm
Operating Wavelength	~840 nm	~840 nm	~1060 nm
Scanning Mirror Type	Galvanometer	Galvanometer	2D MEMS
Dimensions (L x H x W)	23 cm x 18 cm x 8 cm (including lens)	28 cm x 32 cm x 14 cm	15 cm x 18 cm x 7 cm (Power Grip) 16 cm x 10 cm x 14 cm (Camcorder)
Handheld Weight	1.5 kg (with lens)	2.2 kg	0.50 kg (Power Grip) 0.42 kg (Camcorder)
Refractive Error Correction	Manual	Motorized	Manual
Display on Handheld	N/A	LCD Touch Screen	LCD Screen
Alignment Aids	OCT Preview Scans	OCT Preview Scans IR Camera Fixation Target	OCT Preview Scans Iris Camera Fixation Target
Ophthalmic Imaging	Retinal Anterior Segment	Retinal Anterior Segment	Retinal

For an OCT instrument to be used outside of ophthalmology or optometry clinic settings, the cost of the instrument should be reduced. The current cost of SS-OCT would be too high for screening applications assuming the standard business model of non-specialist clinicians purchasing an instrument. The future costs will be determined by many factors including the manufacturing volume and the existence of related large markets which can drive price down for key component technology. The majority of the system cost is currently from the prototype VCSEL laser source and data acquisition electronics. Custom designed A/D electronics can significantly reduce cost compared with commercial high speed A/D boards. In this study, an optically pumped VCSEL was used. The development of electrically pumped VCSELs combined with increased production volumes can reduce the laser source cost. However, it will be challenging to significantly reduce costs in the near term. Because the cost of OCT instrumentation for screening is currently high, alternate business models would be needed in order to allow the public to have access to screening. Business models, such as a pay per use may be possible in order to support a higher initial cost. Higher instrument costs or pay per use may also be justified in high risk patient cohorts, such as the diabetic population, where surveillance would be cost effective for detecting early disease. In general, enabling screening should have a significant impact on public health since there is a high rate of undiagnosed eye disease in certain population subgroups.

Finally it is important to note that the OCT retinal data obtained for this paper was acquired by trained researchers imaging healthy young adults in a controlled laboratory setting. However, the majority of individuals in need of retinal screening would likely be elderly with poor fixation and ocular opacities may result in increased eye motion and reduced image quality. In addition, imaging would have to be performed by personnel with different levels of training, outside of the usual ophthalmology or optometry settings. Studies must be performed to validate the effectiveness of this handheld device for imaging a cross section of individuals that are representative of the screening population and subjects with eye disease in comparison to standard diagnostic testing methods.

5. Conclusion

We developed a wide field of view, ultrahigh speed SS-OCT handheld imaging instrument with a 2D MEMS scanning mirror for ophthalmic retinal imaging. We demonstrated record imaging speed to date in an OCT handheld retinal imaging instrument, enabling volumetric and high definition cross sectional imaging. The ability to acquire volumetric data is an important advance because OCT fundus images can be generated and arbitrary cross-sectional images and topological thickness maps registered to fundus features can be extracted from the volumetric data. Additionally, two orthogonally scanned volumes can be processed to generate a motion-corrected merged volume. This solves two of the major difficulties of handheld instruments, mitigating the requirement of precisely aiming the instrument scan to a specific position on the retina and correcting the combination of operator and subject motion. Furthermore, the use of an iris camera and fixation target in the device was critical for instrument alignment and selection of scan area. The advantages of this system enable it to be applied as an easy-to-use screening tool for retinal diseases. Advancements in handheld OCT technology promise to enable applications outside of the traditional ophthalmology and optometry clinics, in pediatrics, intraoperative, primary care, developing countries and military medicine. Finally, extensions of these handheld OCT design concepts can be utilized in a variety of OCT applications in clinical specialties other than ophthalmology or optometry.